A statistical evaluation of ballistic backmapping for the slow solar wind: The interplay of solar wind acceleration and corotation

Monthly Notices of the ROYAL ASTRONOMICAL SOCIETY

MNRAS **509,** 2390–2403 (2022) https://doi.org/10.1093/mnras/stab2965
Advance Access publication 2021 October 19

A statistical evaluation of ballistic backmapping for the slow solar wind: the interplay of solar wind acceleration and corotation

Allan R. Macneil [1]★ Mathew J. Owens [1]★ Adam J. Finley[2] and Sean P. Matt[3]

[1]*Department of Meteorology, University of Reading, Reading, Berkshire RG6 6AH, UK*
[2]*Department of Astrophysics-AIM, University of Paris-Saclay and University of Paris, CEA, CNRS, Gif-sur-Yvette Cedex F-91191, France*
[3]*Department of Physics and Astronomy, University of Exeter, Exeter, Devon EX4 4PY, UK*

Accepted 2021 October 11. Received 2021 October 3; in original form 2021 August 26

ABSTRACT

Mapping solar wind plasma back to its source is often achieved using the 'two-step ballistic backmapping' method. Solar wind observations are mapped through the heliosphere to the edge of a PFSS model, by assuming a constant speed, radial, plasma flow. Tracing field lines through the model gives the source location at 1 $R_\odot$ The heliospheric mapping component hinges upon the argument that two known sources of error, stemming from solar wind acceleration and non-radial flow, effectively cancel. This assumption has not been tested statistically. In this study, we evaluate the heliospheric portion of two-step backmapping, in addition to mapping using models with explicit radial acceleration, and azimuthal velocity, v_ϕ, derived from angular momentum conservation. We estimate longitudinal mapping offsets, $\Delta\phi$, between 326 Earth-observed crossings of the heliospheric current sheet (HCS), and corresponding crossings at 2.5 $R_\odot$ from PFSS models. While the detailed solar wind models can be optimized to produce $\Delta\phi$ in good average agreement with HCS crossing data, the ballistic mapping performs almost as well, although all residuals have a sizeable standard deviation $\sigma \sim 16^\circ$. We conclude that the proposed error cancellation likely contributes to the good performance of ballistic mapping. However, interplanetary acceleration and the height of effective solar wind corotation are both smaller than previously assumed. Our results further suggest that early Parker Solar Probe observations of large v_ϕ around 36 $R_\odot$ do not represent the overall solar wind, due to the requirement for it to be balanced by increased acceleration.

Key words: Sun: heliosphere – solar wind.

1 INTRODUCTION

1.1 Solar wind mapping

One of the fundamental questions in heliophysics is that of how the solar wind is created in the corona and expands into the heliosphere. A major step towards understanding solar wind formation is the establishment of observational links between solar wind streams encountered *in situ* in the heliosphere and the locations at the Sun where they originate, which are observed remotely. Making this link for specific solar wind streams is important due to the spatial variability of solar wind plasma properties, which depend strongly upon the source region (Krieger, Timothy & Roelof 1973).

Approaches for linking *in situ* and remote sensing domains exist with varying levels of sophistication. These range from matching solar wind and coronal structures (e.g. Krieger et al. 1973; Schwenn et al. 1978; Rouillard et al. 2020a), to simplified solar wind propagation models and schemes (e.g. Nolte & Roelof 1973; Schwenn 1990; Neugebauer et al. 1998; Riley & Lionello 2011; Owens et al. 2020b; Rouillard et al. 2020b), to MHD modelling (e.g. Riley et al. 2019; van der Holst et al. 2019; Kim et al. 2020; Réville et al. 2020). These approaches are frequently focused on estimating the coordinates of a stream's source at the Sun, based on the inferred traveltime, flow properties, and location where it was measured (i.e. mapping). For the purposes of this study, we shall focus on one of the most simple and widely applied mapping approaches: two-step ballistic backmapping (Nolte & Roelof 1973; Neugebauer et al. 1998).

Two-step ballistic backmapping maps spacecraft observations to the Sun by separating the plasma propagation into two parts. First, the solar wind is assumed to flow with a constant, purely radial, velocity, in order to calculate a traveltime, Δt, between the point of solar wind release and the spacecraft. The point of release is taken to be the outer edge of a potential field source surface (PFSS; Schatten, Wilcox & Ness 1969) model of the global coronal magnetic field, typically chosen to be $r_{ss} = 2.5\,R_\odot$. For a spacecraft observing solar wind with radial velocity $v_r = v_{sc}$, located at distance $r = r_{sc}$, $\Delta t = v_{sc}/(r_{sc} - r_{ss})$. From Δt, we compute the corresponding change in heliographic Carrington longitude experienced by the plasma during transit, $\Delta\phi = \Omega\Delta t$, where Ω is the solar sidereal rotation rate. The mapped source surface coordinates are then distance r_{ss}, longitude $\phi_{ss} = \phi_{sc} + \Delta\phi$, and latitude $\theta_{ss} = \theta_{sc}$ (where subscripts *ss* and *sc* indicate source surface and spacecraft, respectively). $\Delta\phi$ from this ballistic step of the mapping is on the order of 40°–80° (roughly corresponding to speeds of 600–300 km s^{-1}).

From the source surface coordinates, the plasma is assumed to travel parallel to the PFSS-generated magnetic field. The plasma origin point is then estimated by tracing magnetic field lines from the

★ E-mail: a.r.macneil@reading.ac.uk (ARM); m.j.owens@reading.ac.uk (MJO)

source surface down to 1 $R_\odot$. Travel time is not a consideration here, because the PFSS model is time stationary. The shifts in longitude (and latitude) associated with tracing the field depend heavily on the mapped source surface coordinates. The shift can be close to 0° for a near-radial field line, or >90° for an overexpanding field line near a coronal hole boundary. The two-step ballistic mapping procedure has been widely applied in studies of solar wind origins, including very recently (e.g. Badman et al. 2020; Berčič et al. 2020; Stansby et al. 2020; de Pablos et al. 2021).

It is well established that the two key assumptions (constant speed and purely radial flow) of the heliospheric portion of the ballistic mapping are incorrect. As argued by Nolte & Roelof (1973), however, these assumptions have systematic effects on $\Delta\phi$ that have the tendency to cancel each other out for observers near 1 AU. To explain these effects, Fig. 1 presents a two-dimensional schematic of Carrington longitude ϕ against distance r for differently propagating solar wind streams. Each stream maps to the same point at the spacecraft from different origin points at the Sun. This schematic is based on fig. 1 of Nolte & Roelof (1973), with some additional information included.

Contrary to the constant speed assumption, an accelerating solar wind is both expected theoretically (Parker 1958) and observed experimentally (e.g. Schwenn 1990; Sheeley et al. 1997; Wang et al. 2000). The mapping for two radially propagating streams, one accelerating and the other travelling at a constant speed, is shown by the pair of dashed lines in Fig. 1(a). Fig. 1(b) shows the corresponding radial velocity, v_r, profiles with r, for both streams, where the two profiles reach both reach v_{sc} at the spacecraft. The constant speed stream corresponds to a smaller $\Delta\phi$ than the accelerating stream. This is because the constant speed stream's average speed during transit is greater than the accelerating stream, leading to a shorter traveltime.

The solar wind also has a tangential velocity component, v_ϕ, of the order of one to tens of km s^{-1} at 1 AU, which is, on average, positive in the direction of solar rotation (Weber & Davis 1967). This flow arises due to angular momentum conservation (Weber & Davis 1967), which we shall discuss further in the next section. The corresponding angular velocity, $\omega = v_\phi/r$, is negligible far from the Sun, but at small r can become comparable to Ω. When mapping a radial solar wind, $\Delta\phi > 0$ in Carrington coordinates because the Sun continues to rotate after the plasma has been 'released'. Introducing a non-negligible $\omega > 0$ in the direction of solar rotation will thus reduce $\Delta\phi$. This can be expressed mathematically by the integral

$$\Delta\phi = \int_{r_{\rm inner}}^{1\ {\rm AU}} \frac{\Omega - \omega(r)}{v_r(r)}\,{\rm d}r. \tag{1}$$

Note that for any r at which $\omega = \Omega$ (i.e. the solar wind is co-rotating with the Sun), the $\Delta\phi$ contribution is zero, so long as $v_r > 0$. Example v_ϕ and corresponding ω are shown in Figs 1(c) and (d). Fig. 1(a) shows the evolution of ϕ for solar wind propagating with these v_ϕ. The $v_\phi = 0$ streams produce a larger $\Delta\phi$ than the $v_\phi > 0$ streams with the same acceleration.

We expect that the 'true' mapping for a solar wind stream will result from both acceleration and $v_\phi > 0$. This true mapping is represented by the solid orange line in Fig. 1(a), which maps to $\phi_{A,R}$ (indicating acceleration and rotation). Disregarding acceleration but maintaining $v_\phi > 0$ leads to mapping to $\phi_{C,R} < \phi_{A,R}$. Meanwhile, setting instead $v_\phi = 0$ the stream maps to $\phi_A > \phi_{A,R}$. We can truncate the mapping of ϕ_A down to $\phi_{A,R}$ by defining some height below which the plasma rigidly rotates with the Sun. We label this the 'effective corotation height', r_{EC}, which approximates the influence of v_ϕ on solar wind mapping. We note that this is not the same as the effective corotation height from the standpoint of solar angular momentum loss, as pointed out by e.g. Pizzo et al. (1983).

If we set both $v_\phi = 0$ and use $v_r = v_{sc}$ (i.e. the propagation used in ballistic mapping), we map to ϕ_C. This falls between $\phi_{C,R}$, and ϕ_A, due to the cancellation of the offsets from disregarding each effect. For the parameters chosen for this schematic, we see that ϕ_C falls closer to the true connection longitude, $\phi_{A,R}$, than either of the other simplified mappings.

The above cancellation effect is what is presented by Nolte & Roelof (1973), who modelled the expected acceleration and rotation, and calculated that $\Delta\phi$ computed from constant speed mapping from 1 AU should be approximately equal to the true $\Delta\phi$ offset, with an associated uncertainty of ±10° due to balancing of acceleration and rotation offsets. Specifically, the acceleration follows a power-law fit to a solution to the Parker solar wind model introduced by Burlaga (1967):

$$v_r(r) = K r^{1/4}, \tag{2}$$

where K is a constant. The rotational component is handled by a broad range of possible effective corotation heights 0.1–0.25 AU (around 21.5–50 $R_\odot$).

Evaluations and improvements upon the two-step ballistic mapping procedure have been made, often focusing on improvements around stream interactions, where excess acceleration occurs between fast and slow streams. Schwenn (1990) proposed a scheme for mapping corotating interaction regions that leveraged momentum balance between streams on either side of the interface. Riley & Lionello (2011) compared the outward ballistic propagation between 30 $R_\odot$ and 1 AU with other forms of propagation, including an MHD solution and an *ad hoc* method for accounting for stream interactions created by Arge & Pizzo (2000). Building on the work of Riley & Lionello (2011), Owens & Riley (2017) developed a one-dimensional, time-stationary, 'upwind' solar wind mapping scheme named 'HUX'. This scheme accounts for stream interactions by solving a highly-simplified form of the fluid momentum equation. Later, the 'HUXt' model was introduced by Owens et al. (2020a) by retaining the explicit time-dependencies in the momentum equation.

Neugebauer et al. (1998) carried out one of the earliest studies to employ the two-step ballistic backmapping technique. One component of this was an evaluation of the ballistic portion of the mapping by comparing the percentage agreement between *in situ* heliospheric magnetic field (HMF) polarity associated with solar wind samples encountered at 1 AU and the source surface polarity at each sample's backmapped coordinates. They found that for the three unique Carrington rotations studied (rotation numbers 1892–94) the greatest percentage agreement was achieved following a $\Delta\phi$ shift 20°–25° in excess of that computed using the radial constant speed mapping. The authors suggested that acceleration and rotation offsets are not as well balanced as was concluded by Nolte & Roelof (1973). From Fig. 1, producing an underestimate would require some combination of the acceleration effect being greater than accounted for by Nolte & Roelof (1973), and/or the rotation effect being smaller (i.e. a lower effective corotation height).

More recent studies have used comparisons of percentage agreement between ballistically mapped *in situ* and PFSS polarity to evaluate PFSS representations of the coronal magnetic field. Koskela, Virtanen & Mursula (2017) did so for four decades of data, finding variation in the optimal source surface height depending on solar cycle phase. Kruse, Heidrich-Meisner & Wimmer-Schweingruber (2021) made similar comparisons, and found that allowing variable ellipticity of the source surface also improves polarity agreement. Koskela et al. (2017) also noted that mapping with solar wind speed

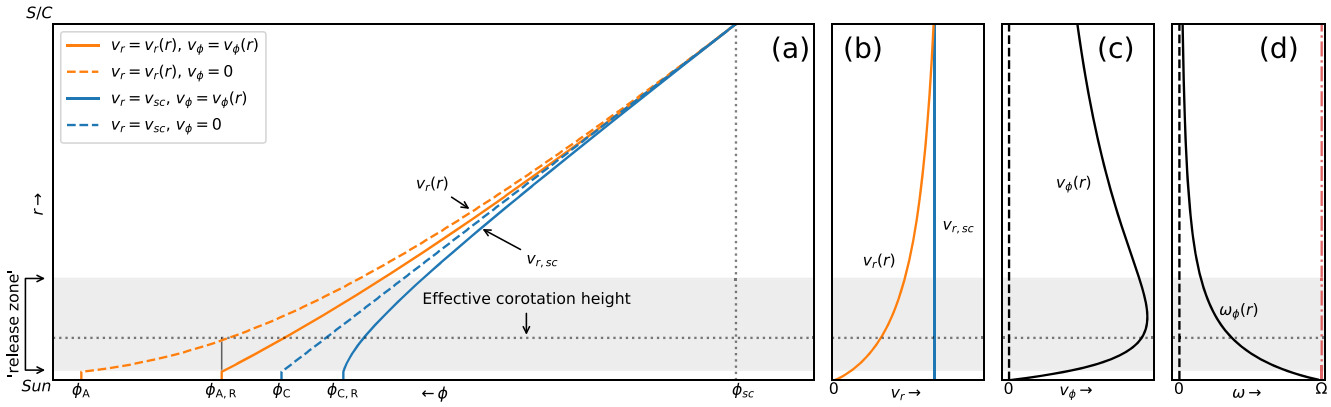

Figure 1. Panel (a): schematic of the evolution of Carrington longitude ϕ as a function of distance r, for solar wind streams with different radial and tangential flow properties. Propagation is shown for four cases, corresponding to combinations of either a constant ($v_r = v_{sc}$) or accelerating $v_r = v_r(r)$ profile, and a zero or radially-dependent v_ϕ profile derived from equation (4), as indicated in the legend. ϕ_{sc} represents the longitude at which a spacecraft encounters the streams. For each stream, $\Delta\phi = \phi_{sc} - \phi_X$, where the subscript X denotes the stream in question. The horizontal dashed line indicates the effective corotation height that is required to reduce $\Delta\phi$ for the accelerating stream with $v_\phi = 0$ down to the same $\Delta\phi$ as the stream that both accelerates and has $v_\phi = v_\phi(r)$. Panel (b): radial velocity profiles $v_r = v_r(r)$ and v_{sc} as a function of r. Panel (c): tangential velocity profiles $v_\phi = 0$ and $v_\phi(r)$ as a function of r. Panel (d): values of angular velocity ω corresponding to the different v_ϕ profiles. The red dot-dashed line shows the angular velocity of the Sun, Ω.

per equation (2) does not perform as well as constant speed mapping. To our knowledge, a more detailed statistical study examining what shifts in $\Delta\phi$ produce best agreement between mapped *in situ* and PFSS polarities, in the vein of Neugebauer et al. (1998), has not yet been carried out.

1.2 Solar wind acceleration

Observations of near-Sun solar wind acceleration have been carried out remotely. Sheeley et al. (1997) measured the radial speeds of slow wind plasma 'blobs' over distances 2–30 $R_\odot$ in coronagraph data. They found acceleration on the order of some 4 m s^{-2}; bringing the solar wind to typical interplanetary speeds of ~ 400 km s^{-1} by around 30 $R_\odot$. Comparable results were found through a similar approach by Wang et al. (2000). The acceleration from these results appears to begin at 0 km s^{-1} at 2–5 $R_\odot$. Outflow speeds derived from solar radio observations also indicate a profile of acceleration in general agreement with these white light observations, subject to a large degree of spread (Wexler, Lawhite & Song 2020a; Wexler et al. 2020b).

Evidence of residual solar wind acceleration at greater distances (0.3–1 AU) has been observed *in situ* by *Helios*. Schwenn (1990) reported 10 and 5 per cent increases in v_r observed by *Helios* 1 and 2, respectively, over these distances. Venzmer & Bothmer (2018) fit the *Helios* velocity observations, binned by r, using a power law, and found the relationship

$$v_{\rm rmed}(r) = Kr^{0.099}, \tag{3}$$

for $v_{\rm rmed}$ the median value of v_r, and $K = 363$ km s^{-1} for the slow wind and $K = 483$ km s^{-1} for the fast wind (split at 400 km s^{-1}). We note that this is the same form as the fit to the Parker solar wind model from equation (2), with a smaller exponent.

Configurations in which *Helios* 1 and 2 were in radial alignment show that while the fast wind exhibits little increase in v_r over 0.3–1 AU, the slow wind residual acceleration is considerable; around 50 km s^{-1} AU^{-1} (Schwenn 1990). This feature arose again in a recent study by Maksimovic et al. (2020), who binned the *Helios* data by distance and v_r quintiles, fitting each quintile linearly with r: $v_r = Ar + v_{r0}$. They found that the gradient A dropped off for increasing v_{r0}, with A ≈ 90 km s^{-1} AU^{-1} for $v_{r0} \approx 250$ km s^{-1} (the lowest quintile) and A ≈ -10 km s^{-1} AU^{-1} for $v_{r0} \approx 620$ km s^{-1} (the highest quintile). For slow wind, a linear fit to equation (2) over the same distance range produces a steeper slope than is derived from these observations, of 131 km s^{-1} AU^{-1}, suggesting that the residual acceleration from the Parker fit may be excessive. Recent Parker Solar Probe (PSP) observations have observed v_r closer to the Sun, and as we would expect for an accelerating solar wind, v_r for the slow wind has access to smaller values at around 30 $R_\odot$ than were typically observed with *Helios* (e.g. Maksimovic et al. 2020; Wexler et al. 2020a).

1.3 Solar wind tangential velocity

Weber & Davis (1967) derived equations for the conservation of solar wind angular momentum per unit mass, which gives rise to the tangential flow profile v_ϕ. From mass conservation and Gauss's law, they went on to produce the following expression for v_ϕ:

$$v_\phi(r) = \frac{\Omega r}{u_A} \frac{u_A - v_r(r)}{1 - M_A^2(r)}. \tag{4}$$

Here, M_A is the radial Alfvén mach number defined as $M_A = v_r/v_A$, where v_A is the local Alfvén speed computed using the radial component of the HMF, B_r, in place of the absolute value B. u_A is the wind speed at the radial Alfvén height r_A, which is the height at which $v_r = v_A$. This formulation allows v_ϕ to be computed from pre-calculated $v_r(r)$ and $v_A(r)$ profiles.

Weber & Davis (1967) computed an example profile of v_ϕ as a function of r resulting from simulating a self-consistent, polytropic solar wind with boundary conditions set to reasonable values observed near Earth. This produced a profile with $v_\phi \approx 1$ km s^{-1} at 1 AU, and a peak value of $v_\phi \approx 4$ km s^{-1} at ~ 20 $R_\odot$. The value of r_A in this solution was 24.3 $R_\odot$.

v_ϕ measurements are considered subject to large uncertainty, because v_ϕ is expected to be small in comparison to v_r, and it is also sensitive to spacecraft tangential velocities and pointing errors (see e.g. Pizzo et al. 1983). Never the less, initial *in situ* observations of v_ϕ were reported to be roughly consistent with the Weber & Davis (1967) predictions. Lazarus & Goldstein (1971) reported v_ϕ observed by

Mariner 5 evolving from around 10 to 1 km s^{-1} over the distance 0.7–1 AU. Having corrected for pointing errors in both *Helios* spacecraft, Pizzo et al. (1983) and Marsch & Richter (1984b), Marsch & Richter (1984a) reported an average $v_\phi = 1.45 \pm 28.11$ km s^{-1} over distances 0.3–1 AU. They found average $v_\phi = 11.82$ km s^{-1} for wind of $v_r < 400$ km s^{-1}, $v_\phi = 1.8$ km s^{-1} for 400 km s^{-1} $\leq v_r \leq$ 600 km s^{-1}, and $v_\phi = -2.2$ km s^{-1} for $v_r > 600$ km s^{-1}. $v_\phi < 0$ in the faster wind was attributed to stream dynamics. The corresponding r_A were reported to be some 34 $R_\odot$ (40–48 $R_\odot$) for the slow solar wind and around 13 $R_\odot$ (13–30 $R_\odot$) for the fast wind. Non-bracketed values correspond to lower limits on r_A inferred only from the magnetic torque contribution to specific angular momentum, while bracketed values were computed by Marsch & Richter (1984a) incorporating the more uncertain particle contributions.

At 1 AU, Finley et al. (2019) computed Carrington rotation-averaged proton v_ϕ using the *Wind* spacecraft. They found these averages exhibit strong variability, around 1–10 km s^{-1}. Based on the distribution of v_r in the ecliptic plane, around 80 per cent of their observations correspond to $v_r < 500$ km s^{-1}, and thus represent the slow solar wind. The remaining 20 per cent of observations, associated with the fast wind, had, on average, a negative v_ϕ, matching the trend observed by the *Helios* spacecraft. Similar values are reported by Němeček et al. (2020), who studied the deflection of the Earth's magnetotail due to non-radial solar wind flows.

PSP has allowed measurement of v_ϕ at unprecedented proximity to the Sun. These observations are naturally more important for mapping, since $\omega = v_\phi/r$. Kasper et al. (2019) reported mean values from the first two PSP encounters of $v_\phi \sim 40$ km s^{-1} at ~ 36 $R_\odot$, measured by the Solar Wind Electrons Alphas and Protons (SWEAP) experiment's Solar Probe Cup (SPC). These are well in excess of those predicted by Weber & Davis (1967), and exceed 50 per cent of rigid rotation velocity at these distances. Despite the estimated values of r_A from these v_ϕ observations being shown to be comparable to the spacecraft distance, the solar wind remained super-Alfvénic. Réville et al. (2020) suggested a resolution to this based on the presence of pressure anisotropies, which increase v_ϕ closer to the mean observed values. With the same data, Finley et al. (2020) noted the presence of strong positive and negative patches of v_ϕ that they suggest, when averaged, can lead to values more consistent with Weber & Davis (1967). Liu et al. (2021) offered an alternative solution in the contribution of alpha particles to the solar wind angular momentum. However, this was not observed by Finley et al. (2021) who used the SWEAP Solar Probe Analyzer (SPAN) to measure the v_ϕ of the proton core, beam, and alpha particle populations, during PSP encounters 3 and 4. Considering the measurements themselves, Woodham et al. (2021) showed that the velocity distribution measured by SPC may be truncated when there is large $-v_\phi$. Their results imply larger $-v_\phi$ values than initially thought, which would decrease the large, positive, v_ϕ averages.

The larger values of v_ϕ measured closer to the Sun mean that the tangential velocity component is a more significant fraction of the total speed. This reduces one factor contributing to the overall uncertainty in v_ϕ measurements. In addition, increased accuracy in the spacecraft pointing (in part due to the inclusion of remote-sensing instrumentation) has allowed for accurate measurements of v_ϕ to be carried out with Solar Orbiter (SO) at an increased heliocentric distance (Verscharen et al. 2021). Like previous observations, they detect both positive and negative values of v_ϕ, which have a distinct trend with radial wind speed. Ultimately, values measured *in situ* can be much larger (or lower) than those depicted by Weber & Davis (1967).

1.4 Testing ballistic mapping

Given the reported observations of large and variable v_ϕ that depart from the model of Weber & Davis (1967), and the likelihood that the residual acceleration from equation (2) is too large, it is appropriate to test the suggestion by Nolte & Roelof (1973) that the assumption of cancellation of errors due to the constant speed, radial, solar wind mapping is valid. This is a key assumption in the ballistic portion of the widely applied two-step ballistic mapping procedure. In this study, we aim to produce a statistical estimate of the true value of $\Delta\phi$ between 2.5 $R_\odot$ and 1 AU using data spanning 14 yr. Our approach is similar to Neugebauer et al. (1998), in that we compare *in situ* magnetic polarity observations to those near the Sun, as derived from a PFSS model. However, we will explicitly compute $\Delta\phi$ for crossings of the heliospheric current sheet (HCS), which we will refer to as $\Delta\phi_{HCS}$, such that our results apply strictly to the slow solar wind. $\Delta\phi_{HCS}$ can then be compared to $\Delta\phi$ computed using the ballistic mapping approach. In order to explain our results, we also model solar wind propagation for different combinations of v_r and v_ϕ radial profiles, and compare the resulting $\Delta\phi$ to $\Delta\phi_{HCS}$. We begin by presenting the data and methods used to produce these results in Section 2, before showing the results themselves in Section 3. We discuss the implications for solar wind mapping and propagation in Section 4, and present our conclusions on these in Section 5. A pair of appendices provide additional information and figures to support the study.

2 DATA AND METHODOLOGY

2.1 *In Situ* data

We identify HCS crossings and corresponding plasma properties near Earth using *in situ* hourly-averaged plasma and magnetic field data from the OMNI data set (available at https://omniweb.gsfc.nasa.gov/ow.html) for the period spanning 2006 October 19–2020 December 31. Supporting observer heliographic distance r, latitude, θ, and longitude ϕ information for these data are obtained from the Earth ephemeris included in the SUNPY package (Mumford et al. 2015).

2.2 HCS detection

To identify times and heliographic coordinates of HCS crossings in the OMNI data, we begin with the sector boundary list from L. Svalgaard (available: http://wso.stanford.edu/SB/SB.Svalgaard.html). This list is algorithmically generated through a combination of *in situ* HMF and ground-based measurements and specifies dates of boundary crossings, as well as the sign of the HMF polarity change, and the wait time until another crossing on either side of the boundary. From this initial list, we discard any crossings that have fewer than 4 d on either side without another sector boundary (this criteria is loosely followed in the original list). For the specified time period, this list yields 396 sector boundary crossings; about two to three crossings per Carrington rotation.

We design an algorithm that identifies a more precise HCS crossing time corresponding to each sector boundary, and discards crossings where this is not possible. We first compute ψ_P, the smallest angle between the $R - T$ component of the HMF vector (RTN coordinates) and the nominal Parker spiral angle, calculated using the radial solar wind velocity component v_r. From this, we define the HMF polarity $B_P = 1\,(-1)$ for $\psi_P < 90^\circ$ ($\geq 90^\circ$). For each sector

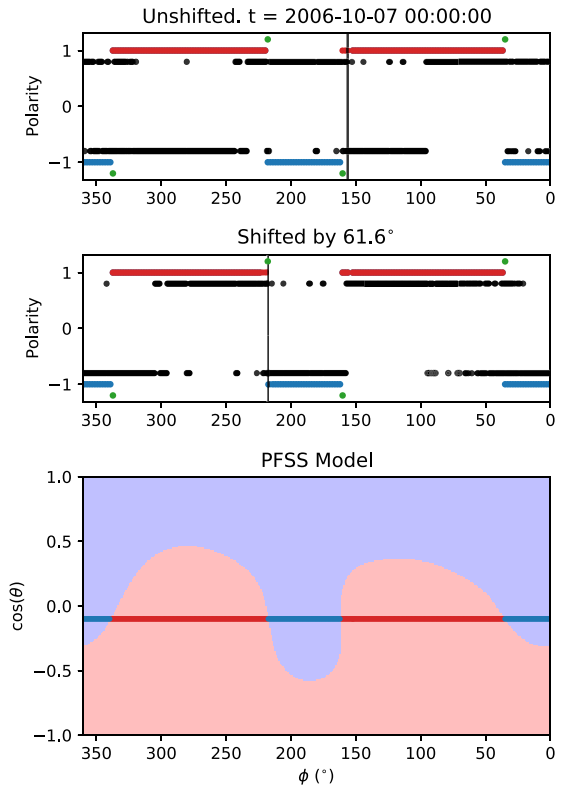

Figure 2. Example of HCS matching procedure. Top panel: magnetic field polarity against heliographic longitude, ϕ. Black points correspond to *in situ* measurements. The black vertical line indicates the location of the *in situ* HCS crossing from which the shift is computed. Blue and red points correspond to expected polarities derived from the PFSS model (bottom panel). Green points indicate the identified polarity reversals from these data. Middle panel: the same as the top panel, but *in situ* data are shifted in ϕ to produce agreement between the HCS and PFSS reversal longitudes per the method detailed in Section 2. Bottom panel: PFSS model used for this example. Red and blue points are positioned along the projected spacecraft trajectory, and coloured based on the polarity of the source surface field at that location.

boundary crossing, we consider B_P during the period corresponding to 3 d either side of the crossing date. We fit this B_P as a function of time using a logistic regression (e.g. Wasserman 2004), to identify the decision boundary in time that best separates the positive and negative regions of B_P. The location of the decision boundary is interpreted as the time of HCS crossing in the magnetic field data. To eliminate samples with ambiguous polarity, we only include samples for which $|\psi_P - 90^\circ| > 25^\circ$ in the regression procedure. The top panel of Fig. 2 shows an example HCS detection for the black points that show observed B_P.

A product of logistic regression is the accuracy score, which, in this case, quantifies the fraction of B_P samples correctly predicted by the fitted decision boundary. A low score indicates that the fitted decision boundary often fails to produce a prediction at a given time that matches B_P. Most commonly this is because B_P flips from 1 to −1 multiple times. We discard crossings with a regression score <0.8 (chosen by inspecting numerous crossings) on the basis that such a score indicates an HCS that is extended or ragged, such that its location cannot be appropriately described by a single time stamp or longitude location. We further discard crossings where < 50 per cent of the samples meet the $|\psi_P - 90^\circ| > 25^\circ$ condition; where > 90 per cent of the samples in the 6-d interval are of the same polarity; or where the fitted HCS crossing time is ≥ 2 d removed from the date reported in the initial list. Following this procedure, there are 326 HCS crossings remaining with valid crossing times.

2.3 Coronal current sheet identification

To estimate the location of the current sheet at the Sun, we employ GONG synoptic magnetograms (available at https://gong2.nso.edu/oQR/zqs/) as the inner boundary of a PFSS model for each *in situ* HCS crossing. GONG synoptic magnetograms are available beginning 2006 September 19, which constrains the time periods available for study. For each HCS crossing, we obtain the synoptic magnetogram labelled with the time corresponding as near as possible to the *in situ* crossing time. Given the expected slow wind traveltime of 3–4 d, this ensures that the photospheric field around the region likely underlying the HCS's solar origin (i.e. westward of the observer's meridian at the time the HCS is encountered) has been incorporated into the synoptic map since the prior rotation.

From each GONG map, we compute a PFSS magnetic field using the pfsspy software package (Yeates 2018; Stansby 2019). We use a source surface height of 2.5 $R_\odot$, corresponding to the most common choice for two-step ballistic mapping. We extract the magnetic field polarity at the source surface at the θ and ϕ positions of the spacecraft for the 27-d period preceding the *in situ* HCS encounter. This yields a one-dimensional slice of magnetic polarity against ϕ at the source surface. The bottom panel of Fig. 2 shows an example PFSS output at 2.5 $R_\odot$ and the corresponding one-dimensional slice. We algorithmically identify the longitudes of polarity reversals, ϕ_{rev}, from this one-dimensional series as locations where the magnetic polarity changes between adjacent grid points. These are locations where the current sheet intersects the spacecraft trajectory, which will map to HCS crossings *in situ*. We exclude from study any polarity reversals that are <30° from one another to avoid later ambiguity.

2.4 Calculation of crossing offsets

We combine the *in situ* and PFSS polarity reversal to produce an estimate of the longitude offset resulting from solar wind propagation from the Sun to the Earth, $\Delta\phi_{HCS}$. To facilitate this we first match each *in situ* crossing to its likely counterpart from the PFSS data. For each crossing-model pair, we compute the difference between the longitude of the *in situ* HCS crossing ϕ_{HCS}, obtained from the Earth ephemeris, and each identified PFSS polarity reversal, $\phi_{rev,i}$: $\Delta\phi_{HCS,i} = \phi_{rev,i} - \phi_{HCS}$. We rectify these values such that $0^\circ \leq \Delta\phi_{HCS} < 360^\circ$. We pair together each HCS crossing with the PFSS reversal that has the same change in sign, and the smallest value of $\Delta\phi_{HCS,i}$. Doing so identifies the reversal of appropriate sign that occurred soonest prior to (and so at greater longitude than) the *in situ* crossing in question, which we assume to be its counterpart. We record $\Delta\phi_{HCS}$ as the $\Delta\phi_{HCS,i}$ value for each successful pairing.

2.5 Caveats for HCS methodology

A notable assumption of our approach, and the ballistic mapping approach in general, is that the source surface model magnetic polarity at the spacecraft latitude should correspond to the magnetic structure that is encountered near Earth. Outside of interaction regions, the solar wind typically does not feature a strong latitudinal velocity component, so the connection latitude at the source surface is expected to be reasonably accurate.

Our approach to identifying the HCS *in situ* does not account for the finite thickness of the HCS, or for instances where the

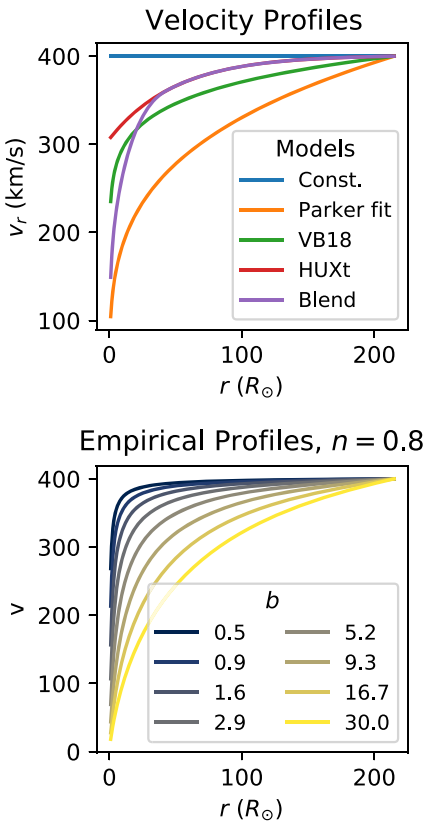

Figure 3. Examples of radial profiles of v_r derived from different models as labelled in the text. Top panel: v_r constant at 1 AU value, fit to the Parker model described by equation (2), the fitted VB18 model (equation 3), empirical v_r model used in HUXt (equation 5), and the 'blended' velocity profile described in the text. Bottom panel: v_r described by a range of coefficients in the asymptotic function in equation (6), with $n = 0.7$, b shown in the figure, and A specified to fix v_r at r=1 AU.

spacecraft crosses back and forth over the same sector boundary. While we exclude many such instances from study through the logistic regression approach, it is possible that some persist and are not properly accounted for. Further, these more complex sector boundaries may propagate differently to the simple ones that we include, which could bias the results in some way.

In interpreting the $\Delta\phi_{\rm HCS}$ estimates, it is important to note that HCS crossings are typically embedded in the slow solar wind. We shall see below that this is supported by the measured radial solar wind speeds associated with the HCS crossings. As such, conclusions which we draw by comparing mapping to $\Delta\phi_{\rm HCS}$, regarding both the expected errors of different mapping approaches and any details of solar wind propagation, apply primarily to the slow solar wind.

2.6 Solar wind propagation

In this study we employ a selection of models for solar wind propagation with which we compute theoretical mapping offsets $\Delta\phi_{\rm M}$. Here we introduce the models of v_r using Fig. 3. The top panel shows a selection of v_r profiles with r, with each profile constructed to reach $v_r = 400\,{\rm km\,s^{-1}}$ at 1 AU. The first model has constant v_r, as assumed in the standard ballistic mapping approach. The model labelled 'Parker fit' is the fit to a solution to the Parker solar wind model introduced by Burlaga (1967) and employed in the work of Nolte & Roelof (1973): equation (2). Similarly, the model labelled 'VB18' represents the power law obtained by Venzmer & Bothmer (2018) from fits to the *Helios* data set over distances 0.3–1 AU described by equation (3). We choose the constant K to fix the speed observed at 1 AU.

The model labelled 'HUXt' represents the empirical acceleration term employed in the HUXt solar wind model introduced in Section 1.1:

$$v_{\rm r}(r) = v_{\rm r0} + \alpha v_{\rm r0}\left(1 - {\rm e}^{-r/r_{\rm h}}\right), \tag{5}$$

where $v_{\rm r0} = v_{\rm r}(r = r_0)$, $r_0 = 30\,{\rm R}_\odot$, $\alpha = 0.15$, and ${\rm r_h} = 50\,{\rm R}_\odot$. These parameter values are tuned by Riley & Lionello (2011) to produce good agreement with 'residual' solar wind acceleration between $30\,{\rm R}_\odot$ and 1 AU, and as a result produce very similar solutions to more sophisticated MHD models (Riley & Issan 2021).

Since the HUXt $v_{\rm r}$ profile is defined relative to $r_0 = 30\,{\rm R}_\odot$, it is not constrained to reach $v_{\rm r} = 0$ at $r = 0$, and possesses large speeds and weak acceleration close to the Sun. We construct a profile that matches the HUXt profile at $r > 30\,{\rm R}_\odot$ but still reaches $v_{\rm r} = 0$ at $r = 0$. We do so by combining it with a profile that obeys equation (2) at $r < 30\,{\rm R}_\odot$, and performing cubic interpolation between the two. We choose K in equation (2) such that its velocity matches that of the HUXt profile at $30\,{\rm R}_\odot$. This profile is labelled 'Blend' in Fig. 3.

To facilitate later analysis, we also construct a formulation for $v_{\rm r}$ that can be tuned more precisely, based on the function

$$v_{\rm r}(r) = A\frac{r^n}{r^n + b}, \tag{6}$$

where A, b, and n are positive free parameters. A specifies the velocity that $v_{\rm r}$ approaches asymptotically, while n controls the growth, and b moderates the rate at which $v_{\rm r}$ reaches A. We ensure that a predefined $v_{\rm r}$ is reached at 1 AU by specifying n and b and then choosing the appropriate value of A. Under these constraints, larger n leads to $v_{\rm r}$ growing rapidly near the Sun. Conversely, larger b causes $v_{\rm r}$ to undergo more of its acceleration further from the Sun, and correspondingly accelerate more gradually close to the Sun. The bottom panel of Fig. 3 shows examples of $v_{\rm r}$ from equation (6), with $n = 0.7$ and a logarithmically spaced range of b.

We account for tangential velocity effects either by assuming purely radial flow above some effective corotation height $r_{\rm EC}$ or by calculating an explicit rotational velocity profile v_ϕ from equation (4). By specifying $r_{\rm A}$, and using the definition $v_{\rm r}(r = r_{\rm A}) = u_{\rm A}$, we compute $M_{\rm A}$ at all r using the relation ${\rm M_A^2} = (v_{\rm r}r^2)/(u_{\rm A}r_{\rm A}^2)$ from Weber & Davis (1967). This relation assumes $\rho v_{\rm r} r^2$ is constant (for mass density ρ), and $B_{\rm r}$ scales as $1/r^2$. To find $\Delta\phi$ during solar wind propagation to 1 AU under combinations of $v_{\rm r}$ and $\omega\,(= v_\phi/r)$ profiles, we simply compute the integral from equation (1). Given the various $v_{\rm r}$ profiles that we consider here, for the sake of consistency and simplicity, we evaluate this integral numerically.

3 RESULTS

In Fig. 4 we present the results of the methodology of Section 2.4 applied to each identified *in situ* HCS crossing to produce estimates of $\Delta\phi_{\rm HCS}$. These data are presented firstly in Fig. 4(a) as a histogram. The histogram produced from all 326 crossings exhibits a clear peak, but with a large spread of values from 0° to 360°. We attribute this spread in large part to errors associated with our boundary matching procedure, in particular the reliance on the PFSS model (see Section 4 for further discussion). We devise a scheme to remove likely erroneous values from further study. Since offsets of $\Delta\phi_{\rm HCS} \geq 180°$ are clearly unrealistic, we eliminate from the study all data that

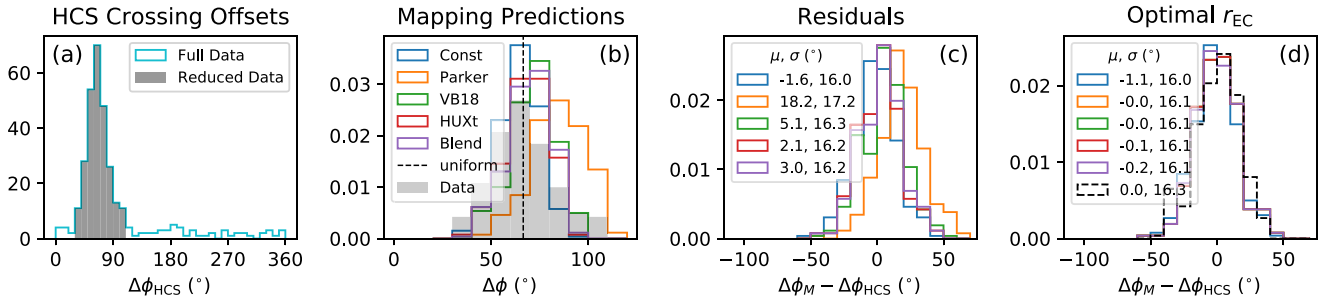

Figure 4. Histograms of results derived from HCS crossing offsets and different mapping procedures. Panel (a): $\Delta\phi_{HCS}$ from HCS crossings described in Section 2.4, both prior to and following the removal of presumed erroneous values. Panel (b): $\Delta\phi_M$ from different solar wind v_r profiles described in the text overlaid on $\Delta\phi_{HCS}$. A vertical line corresponds to the mean optimal offset for a uniformly propagating solar wind. Panel (c): residuals $\Delta\phi_M - \Delta\phi_{HCS}$ for model M used for mapping. Means (μ) and standard deviations σ for each distribution are shown in the legend. Panel (d): same as previous, but with each mapping procedure with effective corotation height adjusted to minimize the mean residual value.

fall into bins containing a number of samples $N \leq N_{>180}$, where $N_{>180}$ is the greatest number of samples in any of the bins located at $\Delta\phi_{HCS} > 180°$. This procedure reduces the number of valid $\Delta\phi_{HCS}$ samples to 261. The remaining data are plotted in the solid grey histogram in Fig. 4(a). This distribution has a mean of 66.°6 and median of 64.°4, and $\sigma = 16.°3$. These correspond to a traveltime mapping at a constant speed of roughly 369 km s^{-1} for the mean and 381 km s^{-1} for the median. The standard deviation in the equivalent speeds is around 90 km s^{-1}.

For each remaining HCS crossing, we calculate an associated v_r by computing the mean v_r value in a 24-h time window centred on the HCS crossing time. The mean (median) v_r for the valid data is 384 km s^{-1} (368 km s^{-1}) – remarkably similar to the average constant radial solar wind speeds derived from travel times corresponding to $\Delta\phi_{HCS}$ above. The true standard deviation in v_r is smaller than inferred from the spread in $\Delta\phi_{HCS}$; around 70 km s^{-1}. We use these speeds to calculate the mapping offsets, $\Delta\phi_M$, using the four v_r models shown in the top panel of Fig. 3, and assuming that the solar wind rotates rigidly with the Sun up to 2.5 $R_\odot$ (the source surface height) and then travels purely radially. For the constant speed case, this represents the standard ballistic mapping approach. We plot histograms of $\Delta\phi_M$ for each model on top of the $\Delta\phi_{HCS}$ histogram in Fig. 4(b). Each mapping produces a distribution of $\Delta\phi_M$ with $\sigma \sim 10°$, which is narrower than that of $\Delta\phi_{HCS}$, reflecting the distribution of v_r as measured at 1 AU for the HCS encounters. The constant speed mapping is roughly in best agreement with the $\Delta\phi_{HCS}$ distribution, in terms of modal values. The other models are shifted to greater $\Delta\phi_M$, since they include acceleration and so exhibit larger travel times. The Parker fit model correspondingly has the greatest shift, while the HUXt and blend models have a smaller shift and very similar distributions, and the VB18 model is intermediate between these.

We compute the distribution of residual values for each model, $\Delta\phi_M - \Delta\phi_{HCS}$, and plot them in Fig. 4. Each residual distribution has a comparable standard deviation, reflecting the broad $\Delta\phi_{HCS}$ distribution and the spread due to the 1 AU v_r measurements. The mean values of the constant speed, VB18, HUXt, and Blend model residuals are all comparatively small, with the constant speed $\Delta\phi$ skewing slightly negative and the others slightly positive. The Parker model skews to a far larger positive value.

We repeat the above process with modelled $\Delta\phi_M$ values re-calculated using effective corotation heights $\geq 2.5\,R_\odot$, which minimize the mean residual values, shown in Fig. 4(d). We also compute and plot the residuals between $\Delta\phi_{HCS}$ and a further simplified mapping approach, in which a uniform mapping offset of $\Delta\phi =$ 66.°6 (found to give optimal agreement) is used. We see that for the accelerating models, it is possible to bring the mean value to effectively zero. For the constant speed model, this is not the case because increasing the corotation height can only decrease $\Delta\phi$. While decreasing the corotation height increases $\Delta\phi$, this would require that we lower r_{ss} in the PFSS model. Doing so would have consequences for mapping between the source surface and photosphere that are beyond the scope of this study. The values of the optimal corotation heights will be investigated below. The standard deviations, σ, are very similar for each residual histogram, including the highly simplified uniform-offset model, for which σ is only slightly larger than the rest.

Fig. 5 presents 'box and whisker' plots that demonstrate the effect of varying the effective corotation height on the residual values of $\Delta\phi_M - \Delta\phi_{HCS}$ for four of the above five solar wind models. The HUXt model is excluded because it appears near-identical to the Blend model. These plots demonstrate that increasing the effective corotation height decreases the $\Delta\phi_M$ value calculated in the mapping. Rough values of 'optimal' effective corotation heights, r_{opt}, become clear for each model, and we estimate precise values of r_{opt} using linear interpolation. We find an r_{opt} of 32.4 $R_\odot$ for the Parker model, 15.0 $R_\odot$ for the VB18 model, and 9.78 $R_\odot$ for the Blend model. The optimal height for the constant speed model lies at $r < 2.5\,R_\odot$, which is invalid since 2.5 $R_\odot$ is our chosen source surface height. These values of r_{opt} are used to generate the optimal histograms shown in Fig. 4(d).

A more realistic representation of the solar wind tangential flow is given by the conservation of angular momentum, as represented by equation (4). We now present comparisons between $\Delta\phi_{HCS}$ and the simulated mapping offset $\Delta\phi_{emp}$. $\Delta\phi_{emp}$ is computed with equation (1) using the empirical asymptotic v_r models (equation 6), and v_ϕ computed according to equation (4), using these v_r with specified r_A. The explored range of r_A extends up to unrealistically large values ($> 50\,R_\odot$). This is motivated by the need to produce the desired v_ϕ profiles (Appendix A) that can approach the enhanced v_ϕ values often observed *in situ* near the Sun (Section 1). In this way, r_A here serves primarily as a mechanism with which to tune v_ϕ, rather than as a physical parameter. Fig. 6(a) plots maps of the mean of the residuals $\Delta\phi_{emp} - \Delta\phi_{HCS}$. Each panel computes the mapping using v_r with a set value of n, with the mean residual plotted against b and r_A. For each of the chosen parameters, a line of zero mean residual is clear. This line falls at greater values of b, indicating more acceleration at larger distances, for greater values of r_A, indicating larger rotational flows. Likewise, this line shifts to lower values of r_A

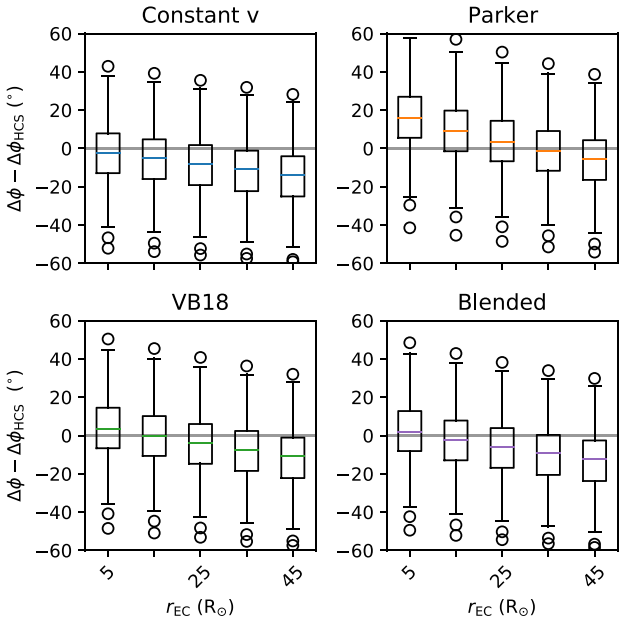

Figure 5. Box and whisker plots summarizing the residuals between $\Delta\phi_{HCS}$ and four of the five the models summarized in Fig. 4, as a function of effective corotation height. For each corotation height, the central lines represent the median value, the box extends from the lower to upper quartile values, the whiskers extend from the box edges by 1.5 times the inter-quartile range, and individual points show samples that lie beyond the whiskers.

for greater values of n, which correspond to weaker rotational flows and stronger acceleration near the Sun, respectively. In Appendix A, we show the curves of v_r and v_ϕ against r for the combinations of parameters that fall along the line. We also find that the mean residual appears to saturate at around -1.5 at low b, for all n and r_A. We plot ticks on the top of each panel of Fig. 6(a), which indicate the perihelion distances of PSP's encounters thus far. To our best knowledge, no encounters with publicly available data (which are all but the innermost) suggest PSP to have definitively crossed r_A (e.g. Liu et al. 2021).

Fig. 6(b) shows maps of the standard deviation, σ, of $\Delta\phi_{emp} - \Delta\phi_{HCS}$ calculated using the same parameters as Fig. 6(a). σ does not vary strongly over the full parameter space shown here. Around the line delineating the smallest mean residual, $\sigma \sim 16.^\circ 2$, which is very similar σ values to distributions in Fig. 4. σ here does not depend strongly on the model parameters b, n, or r_A, indicating that the spread in $\Delta\phi_{emp}$ is dominated by the spread in v_r (which we account for by varying A) associated with the HCS crossings. This occurs because the values of $\Delta\phi_{emp}$ from our model depend approximately linearly on v_r at 1 AU for fixed n, b, and r_A.

Finally, Fig. 7 shows the effective corotation height, r_{EC}, corresponding to a selection of v_r (derived from equation (6) with a range of b, or equation (2)) and v_ϕ profiles (specified by v_r and r_A in equation (4)). v_r here is constrained to be equal to 370 km s^{-1} at 1 AU, based on the median value of solar wind speed for the non-discarded HCS crossings. For each v_r-v_ϕ combination, r_{EC} is defined as the height for which solar wind propagating at v_r, and with angular velocity $\omega = \Omega$ for $r \leq r_{EC}$, $\omega = 0$ for $r > r_{EC}$ (i.e. rotating rigidly out

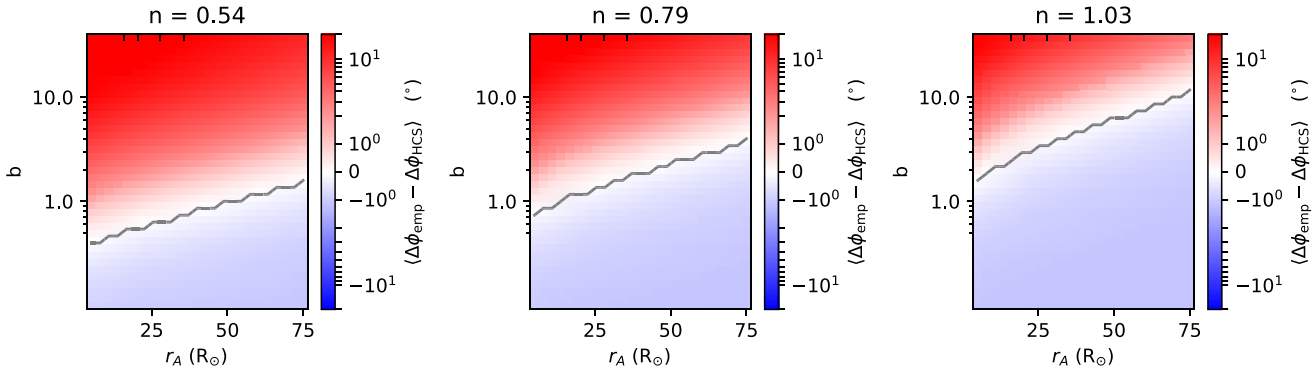

(a) Heatmap of the mean of the residual $\Delta\phi_{emp} - \Delta\phi_{HCS}$.

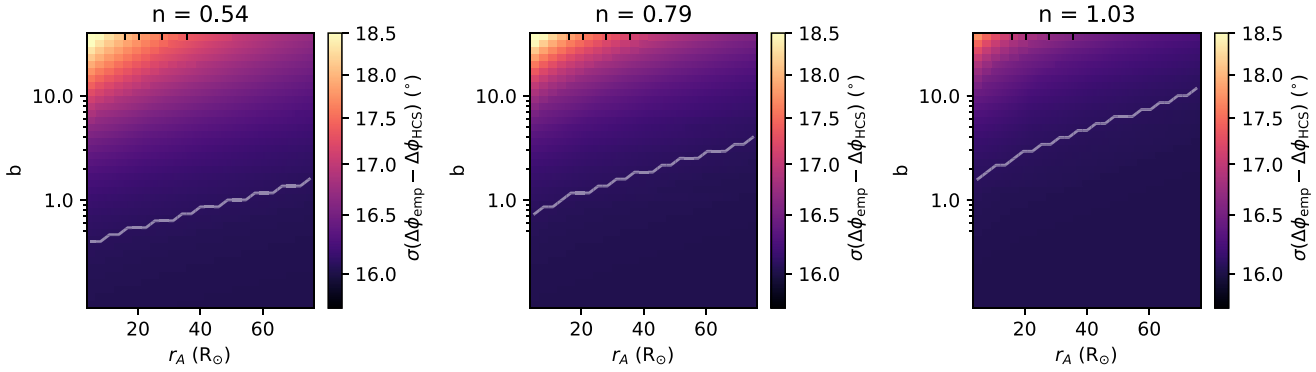

(b) Heatmap of the standard deviation of the residual $\Delta\phi_{emp} - \Delta\phi_{HCS}$. The line of minimum absolute mean residual from 6a is shown in white.

Figure 6. Heatmaps showing properties of the residuals $\Delta\phi_{emp} - \Delta\phi_{HCS}$ for a range of empirical solar wind model parameters. v_r is set using b shown along the y-axes, n corresponding to each panel, and A set to match the model to v_r observed at 1 AU during each HCS crossing. v_ϕ is determined using this v_r and r_A per the x-axes of each plot. Ticks along the top of each panel show perihelion distances for the first nine encounters of PSP.

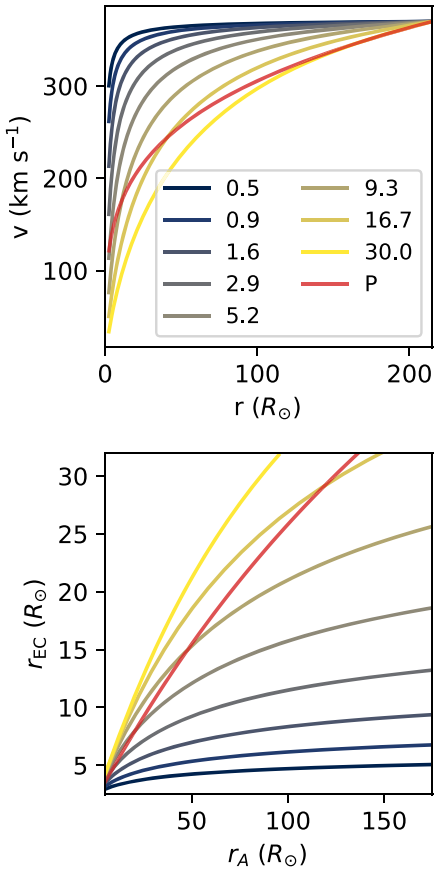

Figure 7. Curves demonstrating the relationship between effective corotation height, r_{EC}, and r_A for a range of v_r profiles generated using either equation (6) with $n = 0.8$ and b given in the label or the Parker fit model (labelled 'P'). The top panel shows each v_r profile, and the bottom panel shows the corresponding relationship between r_{EC}, and r_A, computed as described in the text.

to a given distance and then travelling purely radially), has mapping offset $\Delta\phi$ equal to that computed using v_r and v_ϕ. This is equivalent to the labelled effective corotation heights in Fig. 1. Fig. 7 shows that increasing r_A produces larger v_ϕ, corresponding in general to larger effective corotation heights. For the v_r profiles shown here, and $r_A > 20\,R_\odot$, r_{EC} is between around 10–50 per cent of r_A. Moving to larger r_A, we see that r_{EC} tends to tail off in its growth.

The r_{EC}–r_A relationship depends strongly on v_r. For increasing b, growth in v_r is concentrated at larger r. This leads to larger r_{EC} values required to match $\Delta\phi$, because of the associated increase in v_ϕ, which follows from equation (4). r_{EC} computed using the Parker profile for v_r lies somewhat intermediate between the curves for the smallest and largest b.

4 DISCUSSION

4.1 Solar wind mapping

The results of Section 3 are favourable for the performance of constant speed, radial, solar wind mapping, $\Delta\phi_{con}$, which is central to the two-step ballistic backmapping method. On average, $\Delta\phi_{con}$ from this scheme underestimates $\Delta\phi_{HCS}$ inferred from current sheet crossings by around 1°.5. However, there is a large $\sigma \sim 16°$ in the distribution of the residual $\Delta\phi_{con} - \Delta\phi_{HCS}$, which is nearly identical to σ for $\Delta\phi_{HCS}$ itself. Thus, while the constant speed mapping predicts the central value of $\Delta\phi_{HCS}$ well, it does not account for the spread, which probably arises due to a range of uncertainties, including those discussed below in Section 4.2.

The specified, accelerating, solar wind models (Parker, VB18, HUXt, and Blend) can be adjusted to have close to zero mean residual $\Delta\phi_M - \Delta\phi_{HCS}$, when an optimal effective corotation height is chosen from Fig. 5. While these accelerating v_r configurations are more faithful to the true solar wind propagation, they do not greatly improve upon $\Delta\phi_{con}$, since it already has close to zero mean residual. As in Fig. 1, the constant speed mapping predicts a slightly too small $\Delta\phi$ on average. Introducing acceleration shifts $\Delta\phi$ higher, and it is then brought back down by increasing the effective corotation height, r_{EC}, as shown in Figs 4(d) and 5. This is, in essence, the cancellation of errors presented by Nolte & Roelof (1973).

Crucially, none of the models with optimized r_{EC} in Fig. 4 produce a standard deviation, σ, in the residuals that is noticeably smaller than corresponds to $\Delta\phi_{con}$. This is also true if we consider σ for $\Delta\phi_{emp} - \Delta\phi_{HCS}$, where $\Delta\phi_{emp}$ is derived from the more sophisticated acceleration-rotation models shown in Fig. 6, along the line of zero mean residual. Compared to the other models tested here, then, our results suggest that the constant speed approach is very close to the best-case mapping for tracing the slow solar wind back from 1 AU to the source surface.

We recall from Section 1 that, in a similar study, Neugebauer et al. (1998) found an average shift of an additional 20°–25° over $\Delta\phi_{con}$ gave the best agreement between 1 AU and source surface magnetic polarity. This could arise from methodological differences. For example, this study explicitly compares longitudes of HCS crossings, and thus mapping results apply only to slow wind plasma. Meanwhile, the Neugebauer et al. (1998) study compared the total percentage polarity agreement over an entire Carrington rotation. Further, the present study covers more than a full solar cycle's worth of data from 2006 to 2020, while Neugebauer et al. (1998) covered four consecutive Carrington rotations during 1995, in the declining/minimum cycle phase. Given that the coronal magnetic field will be highly correlated over consecutive rotations, the apparently systematic 20°–25° offset may be in fact a correlated random error (since the spread in $\Delta\phi_{HCS}$ in Fig. 4 shows that a random offset of 20° is very plausible).

4.2 Mapping uncertainty

Here we discuss the sources and implications of errors and variance in our $\Delta\phi_{HCS}$ and $\Delta\phi_M - \Delta\phi_{HCS}$ residual results. In Section 3 we found that mapping with more sophisticated models of solar wind propagation, which include acceleration and corotation, gives standard deviations σ in the residuals that are very similar to the constant speed, radial, mapping. The reason for this is that each of our propagation models produce $\Delta\phi_M$ for a given HCS crossing that is proportional to the observed v_r at 1 AU (e.g. equation 6). These different models, which all have the same distribution of v_r at 1 AU, thus cannot have different spreads in the residual $\Delta\phi_M - \Delta\phi_{HCS}$. Following from this point, it might be possible to reduce the size of σ in residuals for the more sophisticated solar wind propagation models using a more bespoke mapping procedure, in which different acceleration (e.g. from adjusting the b and n parameters in equation 6) and v_ϕ profiles (e.g. adjusted r_A) are used dependent on the observed *in situ* solar wind properties. This would require a detailed fitting procedure over a large parameter space, but may be worthwhile in particular for v_ϕ which has strong observed variability, even when considering only slow wind streams (e.g. Finley et al. 2019; Verscharen et al. 2021). However, given that much of this variability,

particularly between streams with large positive or negative v_ϕ, is observed near to the Sun (Finley et al. 2020), reconstructing v_ϕ profiles based on 1 AU observations may not be feasible, especially if these flows tend to equilibriate before reaching such distances.

The standard deviation, σ, in $\Delta\phi_{\rm HCS}$ results from various contributions. We expect some contribution due to variability in solar wind propagation, particularly differences in $v_{\rm r}$, due to its influence on traveltime. However, computing residuals $\Delta\phi_M - \Delta\phi_{\rm HCS}$ for different solar wind propagation models produces distributions with only a very slight decrease in σ compared to $\Delta\phi_{\rm HCS}$. If $v_{\rm r}$ strongly influenced $\Delta\phi_{\rm HCS}$ in the way it does $\Delta\phi_M$, then we would expect $\Delta\phi_M - \Delta\phi_{\rm HCS}$ to have a greater decrease in σ, since σ for the different $\Delta\phi_M$ is dominated by $v_{\rm r}$. Conversely, if $v_{\rm r}$ was uncorrelated with $\Delta\phi_{\rm HCS}$, such that σ in the residual $\Delta\phi_M - \Delta\phi_{\rm HCS}$ resulted from adding in quadrature those in $\Delta\phi_{\rm HCS}$ and $\Delta\phi_M$, then we would expect an increase in σ up to $\sim 19^\circ$. Our results then suggest $v_{\rm r}$ at 1 AU has a weak influence on $\Delta\phi_{\rm HCS}$ in comparison to other effects, and that the spread in $\Delta\phi_M - \Delta\phi_{\rm HCS}$ must arise either due to inadequacies in how we account for $v_{\rm r}$ in our models, or from other sources, discussed below.

Large and variable v_ϕ near the Sun could produce differences in propagation amongst the different HCS-embedded slow wind streams studied here. These differences would have a strong impact on the distribution of true mapping offsets $\Delta\phi$, and would not be captured by the simple Weber & Davis (1967) approach used in this study. This effect could then constitute a sizeable contribution to σ for $\Delta\phi_{\rm HCS}$ and the residual distributions. We could model such a process in the future by introducing random perturbations to ensembles of v_ϕ profiles near the Sun, and measuring the resulting spread in $\Delta\phi_M$.

Errors associated with the PFSS model (and the construction of the input photospheric synoptic maps) can also contribute to the spread in $\Delta\phi_{\rm HCS}$. In our methodology, we found discrepancies between HCS crossings from PFSS model realizations and spacecraft observations. For example, in unrealistic longitudinal separations of corresponding crossings (Fig. 4a) or mismatches in the numbers of crossings between model realizations and *in situ* data. A range of effects may lead to these issues. Slight positional offsets of magnetic flux sources at the photosphere produce enhanced or diminished warping in the HCS, altering the location or number of HCS intersections with the ecliptic plane. The choice of $2.5\,{\rm R}_\odot$ as source surface height may also produce inaccurate HCS intersections, given that evidence of a non-constant optimal source surface height has previously been reported (e.g. Koskela et al. 2017; Badman et al. 2020; Panasenco et al. 2020). While the unfiltered histogram of $\Delta\phi_{\rm HCS}$ in Fig. 4(a) shows that the impact of errors in PFSS-*in situ* agreement can be sizeable, we expect no inherent longitudinal bias to exist in them. Thus, our average results should be robust to these errors, particularly as we remove the most severe outliers.

From the above, we conclude that σ for the residuals $\Delta\phi_M - \Delta\phi_{\rm HCS}$ arises due to a combination of PFSS errors, and propagation variance that is not described by the models producing $\Delta\phi_M$. It is thus unsurprising that $\sigma = 16^\circ$ for our residuals while the estimated ballistic mapping error from Nolte & Roelof (1973) was only $\pm 10^\circ$, since their method does not include any PFSS modelling and has limited comparison with data. To isolate the error in only the ballistic portion of the mapping from our results would require some independent estimate of the error contribution arising from the PFSS model.

Our results suggest an error of $\pm 16^\circ$ can be expected between ballistically backmapped HCS crossings and crossings derived from PFSS models at the source surface. It is not possible to generalize this to apply to e.g. general applications of the two-step backmapping procedure because the impact of PFSS errors on HCS locations will not be the same as those for other coronal structures. A $\pm 16^\circ$ error could however be expected if we use a constant speed, radial, solar wind propagation to map *outward* to predict the 1 AU, *in situ*, HCS crossing point from a given PFSS realization, provided we have a reasonable estimate of the 1-AU speed.

4.3 Solar wind propagation

In Fig. 6, we demonstrate that an average agreement with observed $\Delta\phi_{\rm HCS}$ can be achieved by computing $\Delta\phi_{\rm emp}$ using a range of combinations of empirical $v_{\rm r}$ (from equation 6) and v_ϕ (from equation 4) radial profiles. To explain our estimates of $\Delta\phi_{\rm HCS}$, any additional acceleration concentrated in the outer heliosphere (higher b or lower n) must be matched by stronger and/or more extended v_ϕ (here provided by greater $r_{\rm A}$), as shown in the schematic of Fig. 1. These results are obtained using equation (4) with self-consistent $v_{\rm r}$ and $v_{\rm A}$, which suggests that the Weber & Davis (1967) model can be compatible with the observed $\Delta\phi_{\rm HCS}$ for current sheet crossings observed at 1 AU. Whether this is the case in reality depends on which, if any, of the many possible solutions are representative of the real solar wind.

The mean of residuals $\Delta\phi_{\rm emp} - \Delta\phi_{\rm HCS}$ shown in Fig. 6(a) appears to saturate at -1.5, for b values falling just below the line of zero mean residual. This effect is emphasized in these plots due to the logarithmic y-axis. The saturation value of -1.5 is very similar to the mean residual found for the constant speed mapping in Fig. 4, so it appears that $b \to 0$ in this model either cannot produce $\Delta\phi_{\rm emp} < \Delta\phi_{\rm con}$, or $\Delta\phi_{\rm emp}$ at least decreases very slowly when it approaches $\Delta\phi_{\rm con}$. In Appendix B, we compute $\Delta\phi_{\rm emp} - \Delta\phi_{\rm con}$ explicitly and confirm that $\Delta\phi_{\rm emp}$ in the explored parameter space never violates $\Delta\phi_{\rm emp} \geq \Delta\phi_{\rm con}$, given our chosen $v_{\rm r}$ profiles and v_ϕ derived from the model of Weber & Davis (1967). This saturation occurs due to $v_{\rm r}$ approaching a constant speed propagation, and may explain why we observe the constant speed mapping to perform relatively well at predicting $\Delta\phi_{\rm HCS}$. However, we expect the saturation to break down if v_ϕ is greater than predicted by Weber & Davis (1967). Given the large v_ϕ observed in the heliosphere which this implementation of the Weber & Davis (1967) model struggles to explain (Section 1), it is possible that in reality this saturation does not occur.

From the results of the explicit $v_{\rm r}$ and v_ϕ modelling, it is tempting to draw comparison with directly measured $v_{\rm r}$ and v_ϕ values, and critical parameters such as $r_{\rm A}$. However, we largely refrain from doing so here for several reasons. Radial profiles of $v_{\rm r}$ and v_ϕ, particularly close to the Sun, are not well constrained by observation. An average radial profile of v_ϕ is especially difficult to produce due to its strong variability (e.g. Finley et al. 2019). We must thus consider a wide range of plausible values for both $v_{\rm r}$ and v_ϕ. As shown in Fig. 6, and in Figs A1 and A2 in Appendix A, a large range of v_ϕ and $v_{\rm r}$ solutions produce equivalent agreement between $\Delta\phi_{\rm emp}$ and $\Delta\phi_{\rm HCS}$. Further, these solutions are very close to the saturation value associated with constant speed mapping, so the true values of these key parameters could be quite different from those which we consider optimal, without changing the results much. Finally, since questions exist regarding whether the Weber & Davis (1967) model is capable of explaining observed v_ϕ (Section 1), it may also be inappropriate for generating realistic values of v_ϕ for the simulated mapping. This factor motivates our inclusion of a large range of values of $r_{\rm A}$ in Fig. 6. The values of $r_{\rm A}$ that produce our results here, and correspondingly determine v_ϕ, thus may not be close to the true values of $r_{\rm A}$. We note many optimal solutions shown in Fig. 6 feature larger $r_{\rm A}$ than is expected based on e.g. predicted number

density values at 1 AU, which give an upper limit of around 40 $R_\odot$ (Appendix A) and observations of predominantly super-Alfvénic solar wind near the Sun reported so far at the PSP perihelia shown in Fig. 6 (Section 1).

While we avoid most comparison with physical observations, the scale of the large ($\sim 50\,km\,s^{-1}$) average tangential speeds at around 36 $R_\odot$ reported by Kasper et al. (2019) is such that some general statements are possible. If we assume that this tangential speed is maintained closer to the Sun then solar wind plasma would be fully corotational at around 20 $R_\odot$. This would naturally correspond to an effective corotation height, r_{EC}, considerably above 20 $R_\odot$, since $v_\phi \sim 50\,km\,s^{-1}$ at 36 $R_\odot$ corresponds to $\omega \sim 0.7\Omega$, which will still have strong influence within the integral in equation (1). The exact value of the corresponding r_{EC} would depend on how v_ϕ drops off beyond this point. Comparing to Fig. 5 we see that the only model capable of making this r_{EC} compatible with our results is the fit to the Parker solar wind solution. However, since we have already noted that this model exhibits excessive residual acceleration, it appears that our results are incompatible with $v_\phi \sim 50\,km\,s^{-1}$ near the Sun being representative of the majority of solar wind streams, or at least the slow streams in which the HCS is typically embedded. In general, our analysis supports the idea that the solar wind cannot predominantly experience rapid rotation near the Sun, or else solar wind acceleration profiles required to explain $\Delta\phi_{HCS}$ become increasingly unrealistic.

Our main result – that constant speed, radial, solar wind mapping performs well at reproducing solar wind mapping from 1 AU – agrees with the prediction from Nolte & Roelof (1973) that this should be the case. However, there are discrepancies between the present study and theirs, when we consider mapping using the Parker fit v_r profile (equation 2) that was also used by Nolte & Roelof (1973). In this case, we require $r_{EC} = 32.4\,R_\odot$ in order to produce optimal agreement with $\Delta\phi_{HCS}$ (Fig. 5). However, to produce such an r_{EC} with our implementation of the Weber & Davis (1967) model requires very large r_A (beyond the axis shown in Fig. 7). This leads to the question of why Nolte & Roelof (1973) predicted that a smaller r_A in the range of ~0.1–0.25 AU (20–50 $R_\odot$) would be sufficient to produce roughly this same r_{EC}. This disagreement appears to be due to their assumption that r_{EC} is very similar to r_A. However, literature cited to support this (e.g. Brandt 1967) refers to the effective corotation height from the perspective of total angular momentum loss, rather than from the perspective of mapping, being close to r_A. Pizzo et al. (1983) pointed out that this effective corotation height is not equivalent to true corotation out to r_A. Since most of the angular momentum is carried by the field, the extent of actual corotation should be far smaller. Computing r_{EC} as defined in Section 1, and as it appears to be interpreted by Nolte & Roelof (1973), produces the result in Fig. 7 referenced above. Thus, while $r_{EC} = 32.4\,R_\odot$ gives optimal agreement with $\Delta\phi_{HCS}$ for the Parker v_r model and lies within the range of r_{EC} presented by Nolte & Roelof (1973), we argue that such a large r_{EC} (per the definition of this work) is not consistent with the model of Weber & Davis (1967), and is probably unrealistic. v_r profiles featuring weaker residual acceleration than the Parker fit model (Blend and VB18) are based on *in situ* v_r observations, and so likely are more realistic at heights $> r_{EC}$. It is encouraging then that the corresponding optimal r_{EC} values to agree with $\Delta\phi_{HCS}$ (Fig. 5) are also more realistic.

5 CONCLUSIONS

In this study we have estimated the longitudinal offsets, $\Delta\phi_{HCS}$, undergone by a large number of slow solar wind samples associated with HCS crossings between 2.5 $R_\odot$ and 1 AU. We used these $\Delta\phi_{HCS}$ to evaluate mapping offsets resulting from a range of different solar wind propagation models. These included $\Delta\phi_{con}$, the offset derived from constant speed, radial, solar wind propagation, which is central to the widely applied two-step ballistic backmapping technique. Although $\Delta\phi_{HCS}$ is subject to a large degree of spread, we find that on average $\Delta\phi_{con}$ agrees well with $\Delta\phi_{HCS}$, to within 1.5°. The standard deviation in $\Delta\phi_{con} - \Delta\phi_{HCS}$ of 16° is made up of contributions from errors in PFSS-*in situ* agreement and variable propagation effects. We thus conclude that constant speed, radial, solar wind backmapping is as accurate as, and also simpler than, the more complex models tested here at mapping slow solar wind streams from 1 AU back to the Sun. This echoes the conclusions of Nolte & Roelof (1973), but now with the support of a large volume of data.

From computing $\Delta\phi_{emp}$ for model solar wind v_r and v_ϕ, we find many solutions involving the model of Weber & Davis (1967) that reproduce the mean observed $\Delta\phi_{HCS}$. However, these solutions do not outperform the constant speed mapping in terms of accuracy or precision (giving close to the same $\sigma = 16°$) because the variance in all of these models is essentially due only to v_r at 1 AU. To improve upon this may be possible, but would likely require a stream-by-stream approach to modelling the propagation. These results allow us to illustrate that the constant speed, radial, mapping indeed performs well because of the cancellation of errors associated with neglecting both radial acceleration and rotational flows. A saturation effect, which arises in the modelled results and limits $\Delta\phi_{emp}$ to be $\geq \Delta\phi_{con}$, could provide the explanation for why the above error cancellation happens in the real solar wind, if its acceleration is sufficiently rapid. The existence of error cancellation agrees with the explanation put forward originally by Nolte & Roelof (1973). Despite this, we would revise some details of their solar wind modelling, favouring solar wind that accelerates less between 0.3 and 1 AU (based on *in situ* observation of v_r) and correspondingly features a lower effective corotation height (i.e. weaker v_ϕ). Our results suggest that the rapid solar wind rotation seen in early PSP measurements, around $40\,km\,s^{-1}$ (Kasper et al. 2019), cannot be maintained everywhere near the Sun. To allow this, unrealistically large residual solar wind acceleration would become necessary in order to explain the good performance of ballistic mapping found here.

The saturation effect and the wide range of plausible v_r and v_ϕ solutions limit the prospects of using the results of the present study to draw further conclusions about solar wind acceleration or angular momentum, including validating the model of Weber & Davis (1967) as implemented here. However, given that $\Delta\phi$ does depend on these integrated parameters, and can be estimated using our methodology, there are opportunities with future studies to leverage this information to explore these topics. Using better constrained and more realistic profiles, particularly measured close to the Sun, of either one of v_r or v_ϕ to compute $\Delta\phi$ would help to constrain estimates of the other. Further, estimates of $\Delta\phi_{HCS}$ made at a range of heliocentric distances could be combined, to allow comparisons with the results from equation (1) evaluated for different outer limits, constraining different radial sections of v_r and v_ϕ evolution. Both of these suggestions become more realistic as further data are returned close to the sun by PSP and SO.

ACKNOWLEDGEMENTS

Work was part-funded by Science and Technology Facilities Council (STFC) grant numbers ST/R000921/1 and ST/V000497/1, and Natural Environment Research Council (NERC) grant numbers

NE/S010033/1 and NE/P016928/1. SPM acknowledges funding from the European Research Council (ERC) under the European Union's Horizon 2020 research and innovation program (grant agreement No. 682393). AJF is supported by the ERC Synergy grant 'Whole Sun', No. 810218. The authors are grateful to Lloyd Woodham for useful discussions. This research made use of ASTROPY, a community-developed core python package for astronomy (Astropy Collaboration 2013, 2018). This research has made use of SUNPY, an open-source and free community-developed solar data analysis package written in PYTHON (Mumford et al. 2015). This research made use of HELIOPY, a community-developed PYTHON package for space physics (Stansby et al. 2019). All figures were produced using the MATPLOTLIB plotting library for PYTHON (Hunter 2007).

DATA AVAILABILITY

This study made use of publicly available data. OMNI solar wind data are available from https://omniweb.gsfc.nasa.gov/ow.html. The Svalgaard sector boundary list and documentation is available from http://wso.stanford.edu/SB/SB.Svalgaard.html. GONG magnetograms are available from https://gong2.nso.edu/oQR/zqs/. The Earth ephemeris data are included in the SUNPY PYTHON package (Mumford et al. 2015). The code used to retrieve, process, and plot all data used in this study can be obtained from https://github.com/allanrmacneil/sw_map_study.

REFERENCES

Arge C. N., Pizzo V. J., 2000, J. Geophys. Res., 105, 10465
Astropy Collaboration, 2013, A&A, 558, A33
Astropy Collaboration, 2018, AJ, 156, 123
Badman S. T. et al., 2020, ApJS, 246, 23
Berčič L. et al., 2020, ApJ, 892, 88
Brandt J. C., 1967, ApJ, 148, 905
Burlaga L. F., 1967, J. Geophys. Res., 72, 4449
de Pablos D., Long D. M., Owen C. J., Valori G., Nicolaou G., Harra L. K., 2021, Sol. Phys., 296, 68
Finley A. J. et al., 2020, ApJ, 902, L4
Finley A. J. et al., 2021, A&A, 650, A17
Finley A. J., Hewitt A. L., Matt S. P., Owens M., Pinto R. F., Réville V., 2019, ApJ, 885, L30
Hunter J. D., 2007, Comput. Sci. Eng., 9, 90
Kasper J. et al., 2019, Nature, 576, 228
Kim T. K. et al., 2020, ApJS, 246, 40
Koskela J. S., Virtanen I. I., Mursula K., 2017, ApJ, 835, 63
Krieger A. S., Timothy A. F., Roelof E. C., 1973, Sol. Phys., 29, 505
Kruse M., Heidrich-Meisner V., Wimmer-Schweingruber R. F., 2021, A&A, 645, A83
Lazarus A. J., Goldstein B. E., 1971, ApJ, 168, 571
Liu Y. D., Chen C., Stevens M. L., Liu M., 2021, ApJ, 908, L41
Maksimovic M. et al., 2020, ApJS, 246, 62
Marsch E., Richter A. K., 1984a, J. Geophys. Res., 89, 5386
Marsch E., Richter A. K., 1984b, J. Geophys. Res., 89, 6599
Mumford S. J. et al., 2015, Comput. Sci. Discovery, 8, 014009
Němeček Z., Ďurovcová T., Šafránková J., Richardson J. D., Šimunek J., Stevens M. L., 2020, ApJ, 897, L39
Neugebauer M. et al., 1998, J. Geophys. Res., 103, 14587
Nolte J. T., Roelof E. C., 1973, Sol. Phys., 33, 241
Owens M. J., Riley P., 2017, Space Weather, 15, 1461
Owens M., Lockwood M., Macneil A., Stansby D., 2020a, Solar Physics, 295, 37
Owens M. et al., 2020b, Sol. Phys., 295, 43
Panasenco O. et al., 2020, ApJS, 246, 54
Parker E. N., 1958, ApJ, 128, 664
Pizzo V., Schwenn R., Marsch E., Rosenbauer H., Muehlhaeuser K. H., Neubauer F. M., 1983, ApJ, 271, 335
Réville V. et al., 2020, ApJS, 246, 24
Riley P., Issan O., 2021, Frontiers Phys., 9, 268
Riley P., Lionello R., 2011, Sol. Phys., 270, 575
Riley P., Linker J. A., Mikic Z., Caplan R. M., Downs C., Thumm J.-L., 2019, ApJ, 884, 18
Rouillard A. P. et al., 2020a, ApJS, 246, 37
Rouillard A. P. et al., 2020b, A&A, 642, A2
Schatten K. H., Wilcox J. M., Ness N. F., 1969, Sol. Phys., 6, 442
Schwenn R., 1990, Physics of the inner Heliosphere – I. Springer, Berlin, Heidelberg
Schwenn R., Montgomery M. D., Rosenbauer H., Miggenrieder H., Muehlhaeuser K. H., Bame S. J., Feldman W. C., Hansen R. T., 1978, J. Geophys. Res., 83, 1011
Sheeley N. R. et al., 1997, ApJ, 484, 472
Stansby D., 2019, J. Open Source Softw., 5, 2732
Stansby D., Rai Y., Broll J., Shaw S., 2019, Heliopython/heliopy, 10.5281/zenodo.2604568
Stansby D., Matteini L., Horbury T., Perrone D., D'Amicis R., Berčič L., 2020, MNRAS, 492, 39
van der Holst B., Manchester W. B., Klein K. G., Kasper J. C., 2019, ApJ, 872, L18
Venzmer M. S., Bothmer V., 2018, A&A, 611, A36
Verscharen D. et al., 2021, A&A, in press
Wang Y. M., Sheeley N. R., Socker D. G., Howard R. A., Rich N. B., 2000, J. Geophys. Res., 105, 25133
Wasserman L., 2004, All of Statistics. Springer, New York, NY
Weber E. J., Davis Leverett J., 1967, ApJ, 148, 217
Wexler D. B., Lawhite G. M., Song P., 2020a, Res. Notes Am. Astron. Soc., 4, 216
Wexler D. et al., 2020b, Sol. Phys., 295, 111
Woodham L. D. et al., 2021, A&A, 650, L1
Yeates A., 2018, antyeates1983/pfss: First release of pfss code.

APPENDIX A: EXAMPLE RADIAL PROFILES

Figs A1 and A2 show plots of example v_r and v_ϕ profiles, respectively. Each profile corresponds to a combination of b, n, and r_A (for v_ϕ) at a point along one of the lines of minimum mean residual in Fig. 6(a). Each panel corresponds to a panel in Fig. 6(a). These figures show the wide range of v_r and v_ϕ profiles that can produce equivalently optimal agreement with our observed $\Delta\phi_{HCS}$.

Profiles of v_A are derived in Section 2 by assuming mass continuity (constant $\rho v_r r^2$) to give the form of the radial density profiles. In Fig. A3, we plot example density profiles for different profiles of v_r and values of r_A used in the study. To obtain explicit density values, we use the definition of the radial Alfvén speed:

$$v_A^2 = \frac{B_r^2}{\mu_0 \rho}, \tag{A1}$$

where μ_0 is the vacuum permeability, and specify B_r by assuming it scales as $1/r^2$ (per conservation of magnetic flux) and $B_r = 3.5$ nT at 1 AU (i.e. $|B| = 5$ nT for a 45° Parker spiral). We plot number density profiles in Figs A3(b)–(d), which correspond to each v_ϕ–v_r pair shown in Figs A1 and A2. We plot horizontal lines at 1 and 20 cm^{-3} to serve as rough lower and upper limits for realistic number density values at 1 AU. Curves that fall outside of these limits at 1 AU (215 $R_\odot$) suggest sensible r_A limits for the 'optimal' curves in Fig. 6 to be $10 \lesssim r_A \lesssim 40\,R_\odot$. However, these limits are quite sensitive to our initial choice of $|B|$ at r=1 AU.

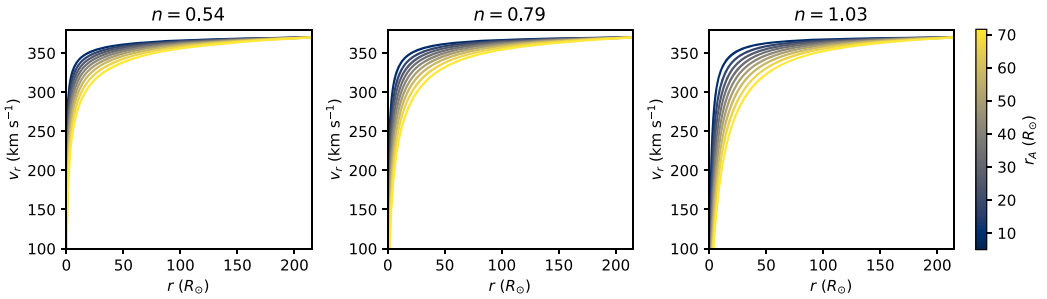

Figure A1. Empirical v_r profiles from equation (6) for example b, n, and $v_r = 370\,km\,s^{-1}$ at 1 AU, drawn from the 'optimal' values of Fig. 6. Each panel corresponds to a different n and line colour corresponds to r_A. The matching value of b can be found by examining the 'optimal' line of b against r_A on the corresponding panel of Fig. 6.

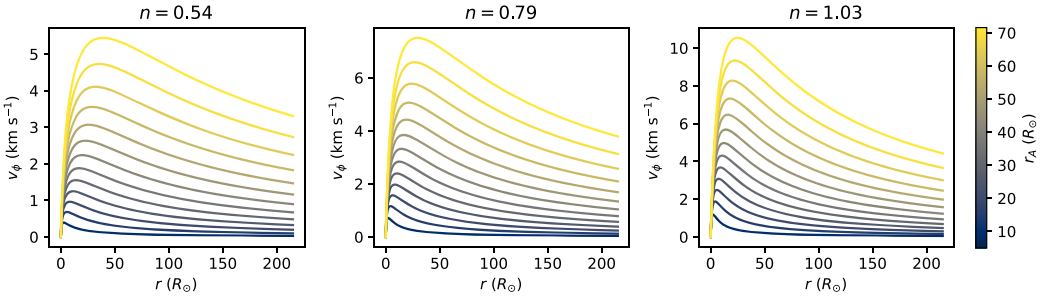

Figure A2. v_ϕ profiles for example b, n, r_A values and $v_r = 370\,km\,s^{-1}$ at 1 AU, drawn from the 'optimal' values of Fig. 6. Each panel corresponds to a different n and line colour corresponds to r_A. The matching value of b can be found by examining the 'optimal' line of b against r_A on the corresponding panel of Fig. 6.

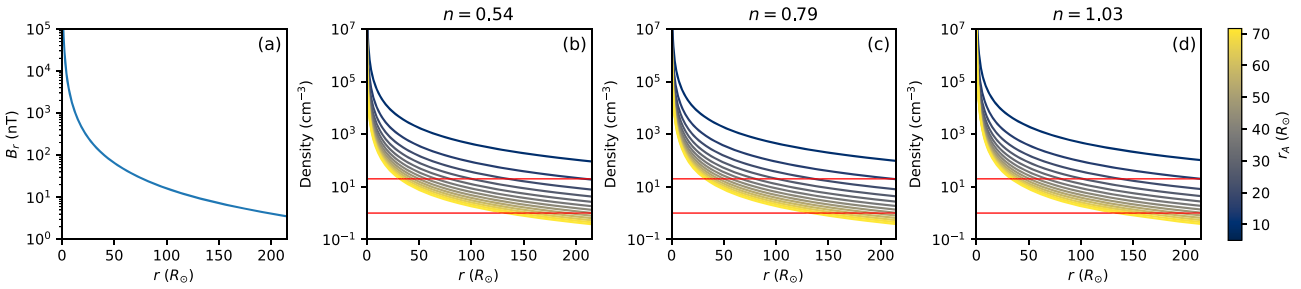

Figure A3. Panel (a): radial profile of modelled B_r used to compute number density. Panels (b)–(d): example density profiles computed using B_r shown in panel (a), for combinations of r_A and v_r computed using equation (6) with parameters specified in Figs A1 and A2. The colour of each density profile corresponds to a different value of r_A, and the corresponding b that controls v_r can be found by comparison with the optimal line in Fig. 6(a). Red horizontal lines correspond to 1 and 20 cm^{-3}.

APPENDIX B: COMPARISON OF EMPIRICAL AND CONSTANT SPEED MAPPING

To investigate the saturation in the mean residual of Fig. 6(a), we compute $\Delta\phi_{emp} - \Delta\phi_{con}$ for the same b, n, and r_A combinations. The result of this is plotted in Fig. B1. We compute $\Delta\phi_{emp}$ only for $v_r = 370\,km\,s^{-1}$ at 1 AU, rather than the distribution of v_r that was obtained from the *in situ* measurements. $\Delta\phi_{con}$ is calculated using the assumptions of $v_\phi = 0$ and a constant $v_r = 370\,km\,s^{-1}$. The minimum value of $\Delta\phi_{emp} - \Delta\phi_{con}$ is 0.3. Fig. B1 shows that $\Delta\phi_{emp}$ in our explored parameter space saturates at $\sim\Delta\phi_{con}$ for small b.

From Fig. 3, v_r approaches the constant speed case as $b \rightarrow 0$, with increasingly rapid acceleration near the Sun. For a model with fixed r_A, this change in v_r increases v_A, resulting in smaller near-Sun v_ϕ from equation (4). The outcome of this is that very little rotational or acceleration effects take place, and $\Delta\phi_{emp}$ tends to the radial, constant speed, case of $\Delta\phi_{con}$. This saturation effect could explain why the constant speed, radial, mapping performs so well on average at predicting mean $\Delta\phi_{HCS}$ (Fig. 4), provided that our modelled v_r and v_ϕ are sufficiently realistic. We also find that it is possible to produce v_r and v_ϕ profiles for which $\Delta\phi_{emp} - \Delta\phi_{con} \leq 0$, if v_ϕ is artificially scaled up from the classical Weber & Davis (1967) values. Thus, it is not fully clear whether the saturation should occur this way in reality.

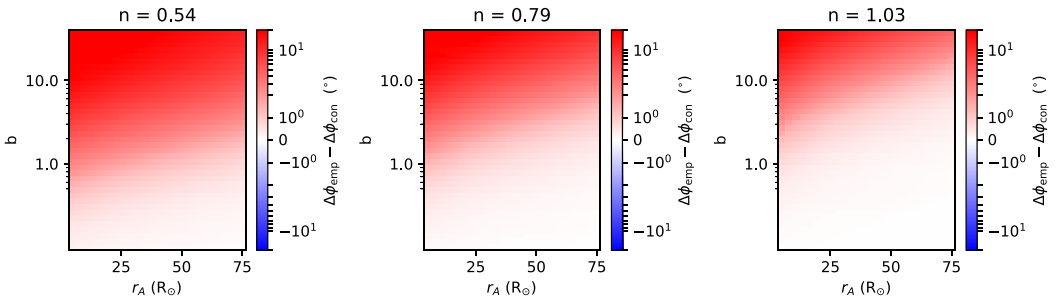

Figure B1. Heatmaps in the form of Fig. 6(a), but showing the residual $\Delta\phi_{\rm emp} - \Delta\phi_{\rm con}$ for different b and n combinations and $v_r = 370\,{\rm km\,s^{-1}}$ at 1 AU.

This paper has been typeset from a TEX/LATEX file prepared by the author.